

Observing quantum coherence from photons scattered in free-space

Shihan Sajeed^{1,2,*} and Thomas Jennewein^{1,2,†}

¹Institute for Quantum Computing, University of Waterloo, Waterloo, ON, N2L 3G1 Canada

²Department of Physics and Astronomy, University of Waterloo, Waterloo, ON, N2L 3G1 Canada

*shihan.sajeed@uwaterloo.ca

†thomas.jennewein@uwaterloo.ca

ABSTRACT

Quantum channels in free-space, an essential prerequisite for fundamental tests of quantum mechanics and quantum technologies in open space, have so far been based on direct line-of-sight because the predominant approaches for photon-encoding, including polarization and spatial modes, are not compatible with randomly scattered photons. Here we demonstrate a novel approach to transfer and recover quantum coherence from scattered, non-line-of-sight photons analyzed in a multimode and imaging interferometer for time-bins, combined with photon detection based on a 8x8 single-photon-detector-array. The observed time-bin visibility for scattered photons remained at a high 95% over a wide scattering angle range of -45° to $+45^\circ$, while the individual pixels in the detector array resolve or track an image in its field of view of ca. 0.5 degrees. Using our method we demonstrate the viability of two novel applications. Firstly, using scattered photons as an indirect channel for quantum communication thereby enabling non-line-of-sight quantum communication with background suppression, and secondly, using the combined arrival time and quantum coherence to enhance the contrast of low-light imaging and laser ranging under high background light. We believe our method will instigate new lines for research and development on applying photon coherence from scattered signals to quantum sensing, imaging, and communication in free-space environments.

Introduction

Quantum coherence is a key ingredient in many fundamental tests and applications of quantum mechanics including quantum communication¹, characterization of single-photon sources², generation of non-classical states³, quantum metrology⁴, quantum teleportation⁵, quantum fingerprinting⁶, quantum cloning⁷, demonstrating quantum optical phenomena⁸, and quantum computing⁹ etc. The ability to transfer quantum coherence via scattering surfaces and its successful recovery from scattered photons enhances several applications of quantum technologies. For instance, quantum communication capable of operating over a scattering channel could accommodate free space communication with non-line-of-sight between multiple users such as indoors around corners, or with short range links with moving systems. Furthermore, the photon coherence recovered from scattered light could be utilized to improve noise performance in low-light and 3D imaging, around-the-corner imaging¹⁰, velocity measurement¹¹, light detection and ranging (LIDAR), surface characterization, or biomedical sample identification.

Currently, the predominant photon encoding used on free-space quantum channels is polarization, because it is not impacted by turbulent atmosphere for clear line-of-sight transmission¹². When photons are scattered, however, their polarization states are inherently disturbed and the quantum encoding is degraded. A previous study¹³ showed that the observed polarization visibility depends on the scattering-surface material, and even the best material (cinematic silver screen) showed a strong dependence on the photon scattering angles with only a total angle of less than 45° was suitable

for quantum communications. Another approach to encode free-space channels is the use of higher-order spatial modes, recently utilized for intracity quantum key distribution¹⁴, yet these photon states are directly impacted by wavefront distortion and are expected to completely vanish upon random scattering from a surface^{15,16}.

Here we utilize quantum coherence encoded in time-bins^{1,17,18} which – although widely used for single-mode optical fibers^{18–22} – has rarely been demonstrated for free-space channels until recently^{23–25}. This encoding is robust upon scattering. The multimode states of light have been utilized using field-widened interferometers, or imaging interferometers, thereby solving the wavefront distortions caused by turbulent media. Such interferometers have the additional benefit of preserving an image. (An alternate approach could be to convert the multimode optical beam back into a single-mode at the receiver by means of adaptive optics, however at the cost of additional losses²⁶). We thus implemented an imaging time-bin interferometer equipped with a single-photon-detector-array (SPDA) sensor, with 8x8 pixels covering a field of about 0.5° . The photon detector achieves high temporal precision of ≈ 120 ps, combined with the ability to spatially resolve the field-of-view with excellent time-bin visibility across the whole sensor area. We demonstrate that our system allows imaging a target that was illuminated with photons prepared with specific phase-signatures, that are recovered from the scattered photons with excellent phase coherence by the illuminated pixels. We discuss the viability of our method in the context of two relevant applications.

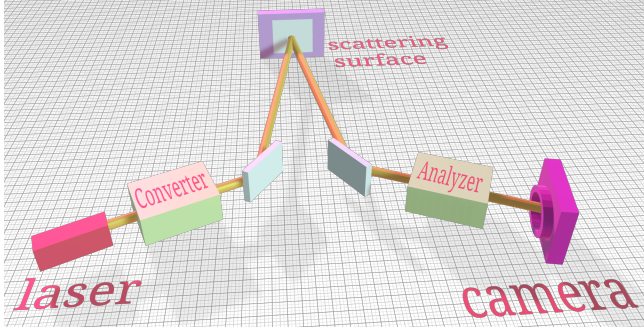


Figure 1. The experimental setup. Optical pulses from a laser are sent through a phase Converter, which creates the initial time-bin states, while the multi-mode Analyzer measures the signals scattered off the target (regular white paper). A single-photon-detector-array is used as the detection device, with 8×8 individual pixels which are time-tagged separately. During the initial alignment, the incident angle = reflected angle = 25° .

Experiment

The experimental setup is shown in Fig. 1 (see Methods for additional details). Each pulse from the laser passes through the Converter – an unbalanced Michelson interferometer (UMI) – that converts it into two coherent pulses separated by a time delay according to the path difference Δ_C . These signals are sent towards the target sample covered with a diffusive material (regular white paper) acting as the *scattering surface*, which can be rotated to vary the angle of incidence. Some of the photons scattered from the surface are captured and guided through the Analyzer, a second UMI with path difference Δ_A . Finally, the photons emerging from the Analyzer are focused into a single-photon avalanche photo-diodes – hereafter referred to as pixels – arranged in a 8×8 row-column configuration, which are free-running and individually time-tagged. Each detected photon could have traversed one of the four possible paths: short-short (SS), short-long (SL), long-short (LS) and long-long (LL) with first (second) letter denoting the path taken inside Converter (Analyzer). The path-differences of the two UMI are tightly matched, i.e., $\Delta_C \approx \Delta_A$, and interference can be observed, as shown in Fig. 2. Piezoelectric actuators are placed at the short arm of each interferometer to vary their respective phase. To compensate for variable angle of incidence and mode-distortion, a 118mm long glass cube with refractive index 1.4525 is placed in the long arm of both interferometers.

A sinusoidal phase difference was introduced between the two interfering (SL and LS) pulses by applying a 0.1 Hz 10V peak-to-peak ramp voltage at the Analyzer piezoelectric actuator (i.e., the length of the *LS* path was varied with respect to *SL*). The resultant outcomes are shown in Fig. 2. The top left columns shows histograms of detection times – with respect to trigger signal – at one of the central pixels (4,4)

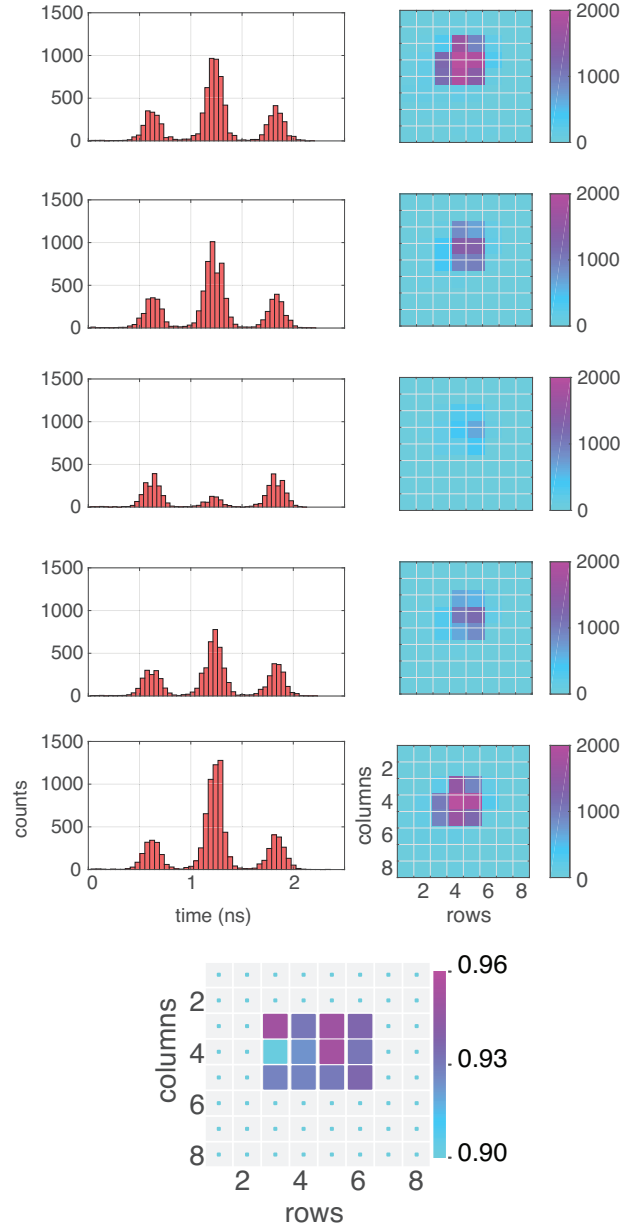


Figure 2. Observed interference. Top left: Histograms of the arrival times of photons at pixel number (4,4) (row 4, column 4). The three separate peaks correspond to photons coming via SS (right), SL or LS (middle), and LL (left) paths (see text for more detail). Five different phase-instances are shown. The visibility at this pixel – calculated by curve-fitting – was $V_{(4,4)} \approx 0.95$. Top right: Middle-peak intensity at the illuminated pixels at the corresponding phase-instances. Bottom: visibilities of the illuminated pixels calculated after fitting the curves. The visibilities range from 0.9 – 0.95. Both the color and the size of the *square* marker in each pixel area are indicators of the visibility. Pixel number (1,1) was used as a trigger. The temporal precision was ≈ 120 ps.

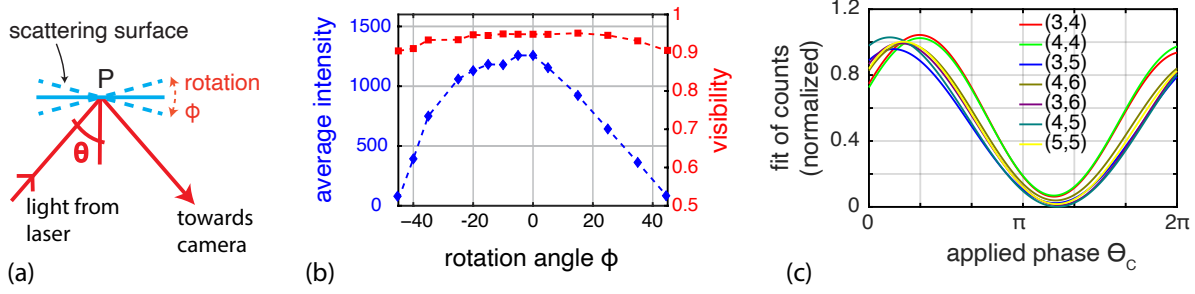


Figure 3. Visibility with scattered light and coherence among the pixels. a. The incident angle θ was varied by rotating the scattering surface about point P by an angle ϕ from -45° to $+45^\circ$ while keeping the position of laser and camera constant. b. Variation of visibility and intensity with rotation angle. Here, rotation angle $\phi = 0$ corresponds to incidence angle of $\theta = 25^\circ$ as shown in Fig. 1. For rotation angles higher than $\pm 45^\circ$, sufficient amount of photon could not be collected by the camera. The average intensity for each angle is shown on the right axis. The collection time for each data point is 20 sec. c. Variation of counts versus phases applied at the Converter for the illuminated pixels. Pixel number (1, 1) was used as a trigger.

(row 4, column 4) for five different phase-instances. The three peaks correspond to photons coming via SS (right), SL or LS (middle) and the LL (left) paths. The temporal precision was ≈ 120 ps. The measured visibility – calculated by fitting the curve – was $V_{(4,4)} \approx 0.95$. The right column shows the corresponding middle-peak intensity for other illuminated pixels. In this case, only the events detected during the 0.6 ns window – centred around the middle-peak – was post-selected. The data collection time was 1 sec for the left and 0.1 sec for the right columns. The visibilities of the illuminated pixels – calculated after fitting the curves – are shown at the bottom which range from 0.9 – 0.95.

Robust and stable phase coherence under scattering angle variations

During the initial alignment, specular reflection was used by setting the incident angle = reflected angle = 25° . We refer to the incident angle as θ . Then, using a rotational mount, the scattering surface was rotated about P to vary θ while keeping the position of the camera fixed (see Fig. 3a). For different rotation angle ϕ , the corresponding average intensity and visibilities are shown in Fig. 3b for pixel number (4, 4). For $\theta = 25^\circ$ ($\phi = 0^\circ$), the majority of photons collected by the camera was due to specular reflection. As $\theta(\phi)$ was varied, the intensity followed the typical scattering pattern consisting of specular and diffusive reflection²⁷. At larger rotation angles ϕ , the collected photons were mainly due to scattering from the diffused surface. For $\phi > |45^\circ|$, the amount of photons collected were too low. However, within the range $\phi \in \{-45^\circ, +45^\circ\}$, although the number of detected photons varied, the visibility remained fairly constant at around 95% with less than 10% variation. The same behaviour was observed for other illuminated pixels.

Recovery of coherence while imaging

As we will demonstrate, this approach offers the unique ability for individual pixels in this imaging analyzer to fully detect the coherence, while at the same time resolving spatial modes

of the scattered photons. To ensure that the camera received mostly scattered photons, the scattering surface was rotated to set $\phi = 20^\circ$ (see Fig. 3a) at which the value of visibility was still close to 0.95. Similar to Fig. 2, only the pixels in the center of the sensor were illuminated. By applying a periodic voltage to the piezoelectric actuator in the Converter interferometer, a sinusoidal phase variation was induced among the outgoing time-bin photons. For each phase θ_c , the corresponding counts at the illuminated pixels were recorded. No voltage was applied at the Analyzer piezoelectric actuator. The fitted count-versus-phase curves for the illuminated pixels are shown in Fig. 3c. The result verified that although each pixel saw a different set of spatial modes of the incoming light, the phase θ_c was preserved by the modes even after going through diffused scattering, and was successfully recovered from the scattered photons by each individual pixel independently. The test was repeated by illuminating all pixels of the SPDA for different scattering angles ϕ , yielding similar results.

Quantum communication with scattered light

We now show the applicability of our setup in implementing quantum communication (QC) with scattered photons in a non-line-of-sight (nLOS) scenario. Here, nLOS refers to the fact that no direct path exists between sender and receiver; neither do they have access to any specular reflector, i.e. mirror surface, at any intermediate point. More specifically, we consider the implementation of the phase-encoded Bennett-Brassard 1984 (BB84) QKD protocol²⁸. The experimental setup was similar to Fig. 1 where the laser and Converter can be considered to be at sender's (Alice's) lab while the Analyzer and the camera at receiver's (Bob's) lab. Photons from Alice's laser were scattered off the diffused surface (white paper) before being measured by Bob. For our experiment, we rotated the scattering surface by $\phi = 20^\circ$ to ensure that photons detected by Bob were mostly due to scattering from the diffusive surface. The four phase-encoded BB84 states

sent by Alice are:

$$|\psi_A\rangle = |e\rangle + e^{i\theta_A} |l\rangle. \quad (1)$$

Here, $|e\rangle$ ($|l\rangle$) denotes the state of the photon that took the early (late) path at the Converter, and $\theta_A \in \{0, \pi/2, \pi, 3\pi/2\}$ is the phase difference applied at the Converter. These states can be generated by applying specific voltages to the piezoelectric actuator placed at the long arm of the Converter. Bob's measurement basis can be chosen by applying phase difference $\theta_B \in \{0, \pi\}$ at the Analyzer piezo actuator. Figure 3c shows the variation of counts versus θ_A at the illuminated pixels for Bob's measurement basis $\theta_B = 0$. Similar variation was observed when Bob's basis was changed to $\theta_B = \pi$ (not shown). The visibilities were in the range of 0.9 – 0.95 for all the illuminated pixels. The result verifies that even though there was no direct line of sight between Alice and Bob, and the photons were being scattered by a diffused surface on their way from sender to receiver, they could still be used for implementing the BB84 protocol with high visibility. Our proof-of-principle implementation makes it an ideal candidate for real-world quantum communication applications over scattering and nLOS channels.

We emphasize that the SPDA sensor enhances the robustness of the QKD receiver, in addition to allowing nLOS operation. Firstly, the imaging information for each pixel can be used for tracking a transmitter beam that feeds into an active beam steering mechanism, or simply used to passively suppress background counts in processing. Secondly, the implementation of multiple photon detector pixels appears to be more robust against certain powerful quantum attacks. For example, the class of detector control attacks^{29,30} could be prevented by adopting the method presented in³¹. The efficiency mismatch type attacks³² – where an eavesdropper attacks by modifying the spatial modes of the incoming light – could be easily detected as changing the spatial mode will change the spatial distribution of detection events.

Low-light imaging in high photon background

It is important to note that the ability to reveal quantum coherence can be directly used to enhance the contrast of an image under a low-light and noisy environment. The experimental setup is similar to Fig. 1, but now the laser focusing condition is adjusted such that all pixels of the SPDA were illuminated. Fig. 4a shows the conventional intensity-based images of the object for four different rotations of the scattering surface. For these tests the scattering surface was rotated to $\phi = 40^\circ$, ensuring that the specular reflection no longer reaches the camera, and the detected photons were only due to diffusive scattering.

A periodic ramp voltage (0.1 Hz, $\pm 5V$ peak-to-peak) was applied to the Converter piezoelectric actuator, to encode a periodic phase-signature pattern among the outgoing time-bin states. The count pattern expected at the SPDA pixels in response to this phase-signature was pre-characterized as shown in Fig. 4b. All the pixels followed roughly the same

pattern. From now on, we shall refer to this as the *reference pattern*.

Figure 4c shows the observed pattern at two neighbouring pixels (4,3) and (4,4). The observed patterns appear distorted due to low SNR, however the correlation with the reference pattern is clearly visible. A similar correlation was observed for all the pixels. However, since bright pixels (such as (4,4)) receive more photons than dark pixels (such as (4,3)) – due to the feature of the object – they are affected less by the noise, i.e., less distorted. This particular feature has been exploited to enhance the contrast as described next.

In order to simulate a noisy low-light environment, the laser was highly attenuated and a lamp was placed in front of the camera to create a high level of background signals. The scattering surface rotation was kept at $\phi = 40^\circ$. The image captured by the imaging array is shown in Fig. 4d. As expected, the presence of high background noise severely degraded the image contrast. The observed pattern in response to applied phase-signature at the same two neighbouring pixels (4,3) and (4,4) are also included in figure 4d. Due to the high background, the DC level of the observed patterns have shifted up considerably, but the correlation with the reference pattern is still visible. For each pixel, we calculated the correlation between the observed and reference pattern (see Methods for more details). We have chosen a threshold of 2.4, and Fig. 4e shows only those pixels having a correlation higher than this value. The result is a reconstruction of the object image with much-enhanced contrast. We note that during measuring the observed patterns, only photons from the SL and LS paths have been considered. In other words, from the three peaks shown in Fig. 2, we only post-selected the detections from the middle-peak which required the timing data for each pixel. As a result, our approach is a combination of utilizing arrival times for coherence analysis, that can also be utilized for LIDAR applications.

We emphasize that instead of intensity, we used the correlation between observed and reference pattern to differentiate the bright pixels from the dark, i.e., instead of choosing an intensity threshold, we chose a correlation threshold. When intensity is used as a detection parameter, the contrast degrades with decreasing SNR. On the other hand, visibility – or more specifically correlation – does not drop as much with decreasing SNR as seen in Fig. 3b. Nevertheless, as a single parameter, visibility cannot generate the image as all the illuminated pixels roughly have the same visibility (see Fig. 6a in Methods). But correlation drops with low SNR as pixels with low SNR are distorted more. As a result, the correlation is an efficient parameter – combined with arrival time data – for imaging an object with enhanced contrast.

We would like to note that the above approach is just a proof-of-principle way to demonstrate how the quantum coherence observed from scattered photons could be used in enhancing the contrast. It is in no way the optimum approach, and better approaches could certainly be devised. For example, the Analyzer interferometer could be realigned to access

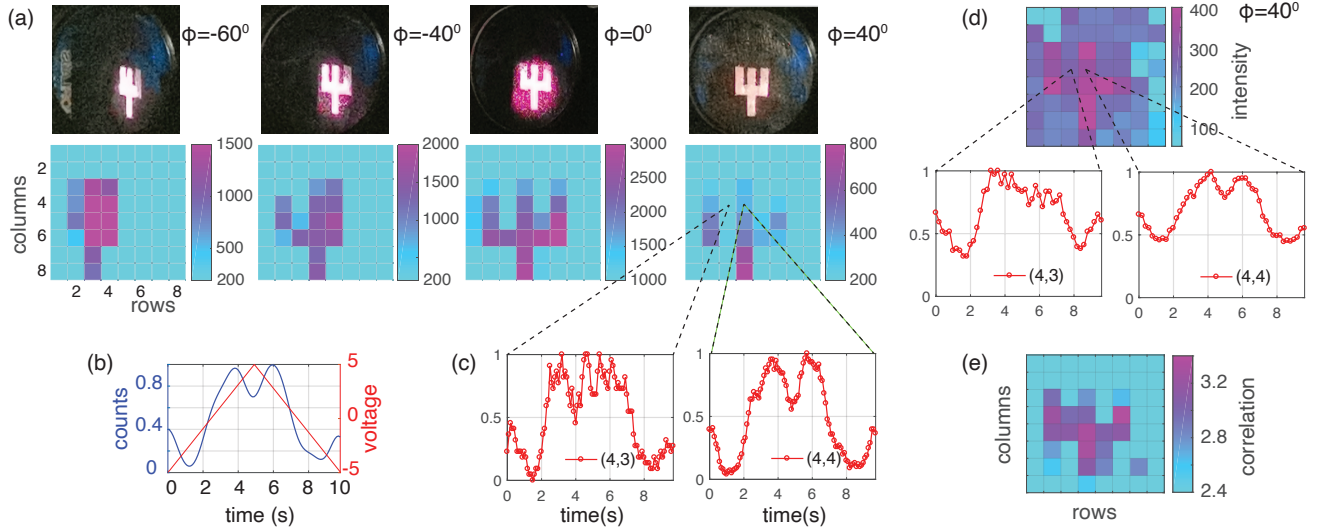


Figure 4. Enhancing the contrast of an image. a. The top and bottom row show the illuminated object (size $4 \times 3.6\text{mm}$) – with the scattering surface rotated at four different angles $\phi \in \{-60^\circ, -40^\circ, -60^\circ, 40^\circ\}$ – and the corresponding images observed in the camera. b. The variation of detector counts as a function of the applied phase-signature. This is the expected count pattern, the reference pattern, for high signal-to-noise ratio scenario. c. The observed pattern in response to the phase-signature for two neighbouring pixels (4,3) and (4,4) for rotation $\phi = 40^\circ$. d. Image captured by the SPDA imager in the low-light and noisy environment. The observed pattern at the same two neighbouring pixels (4,3) and (4,4) are also shown. e. The image reconstructed by cross-correlating the observed pattern with the reference pattern (see text and Methods for more details).

both the outputs having intensity, $P_{\pm}(\Theta) = S_{\pm}(\Theta) + N/2$, with $P_{\pm}(\Theta)(N/2)$ being the intensity (background noise) at the two output arms for a phase difference Θ (here, channel noise is assumed to be equally divided among the output arms). Then, instead of using statistics from a single-arm, measurements from both arms like $P(\Theta) = P_+(\Theta) - P_-(\Theta)$, could be used to nullify the effect of noise to improve the result. However, finding a more sophisticated image-reconstruction method is out of this paper’s scope and will be analyzed elsewhere.

Discussion

This work has demonstrated a novel and robust approach to transfer and recover quantum coherence via scattered photons by realizing a multimode, imaging time-bin interferometer equipped with a single-photon-detector-array sensor. Our quantum receiver achieves excellent temporal precision of ≈ 120 ps as well as the ability to spatially resolve the field-of-view with excellent time-bin visibility across the whole sensor area. Each pixel independently received the coherence from the spatial modes of the scattered photons. The maximum observed visibility was 95%, which remained within a $< 10\%$ variation over a wide scattering angle range of -45° to $+45^\circ$. recovered from photons through a scattering, non-line-of-sight channel. All these features have the potential to open up new avenues in many applications, including quantum communication around-the-corner, low-light and 3D imaging, background noise rejection, around-the-corner imaging¹⁰, velocity measurement¹¹, LIDAR, object detection and identification,

etc.

We demonstrated the application potential of our method by showing two potential applications, one is non-line-of-sight quantum communications, the other is enhancing the contrast of single-photon images. A more detailed and quantitative analysis of these applications will be given elsewhere. We believe our results will instigate further research on the application of coherence in quantum sensing, imaging, and communication and lead to novel areas of application.

Author contribution

S.S. performed the analyses and experiments. T.J. conceptualized the idea and supervised the study. Both authors contributed to writing the manuscript.

Acknowledgement

We thank Duncan England, Bhashyam Balaji, Ramy Tannous, Youn Seok Lee and Alex Kirillova for discussions and technical support. This work was supported by the National Research Council Canada, Defence Research Development Canada, Industry Canada, Canada Fund for Innovation, Ontario MRI, Ontario Research Fund, and NSERC (programs Discovery, CryptoWorks21, Strategic Partnership Grant) and Canada First Research Excellence Fund (TQT).

Disclosures

The authors declare no conflicts of interest.

References

1. Rubenok, A., Slater, J. A., Chan, P., Lucio-Martinez, I. & Tittel, W. Real-world two-photon interference and proof-of-principle quantum key distribution immune to detector attacks. *Phys. Rev. Lett.* **111**, 130501 (2013). URL <https://link.aps.org/doi/10.1103/PhysRevLett.111.130501>.
2. Michler, P. *et al.* A quantum dot single-photon turnstile device. *Science* **290**, 2282–2285 (2000). URL <https://science.sciencemag.org/content/290/5500/2282>. <https://science.sciencemag.org/content/290/5500/2282.full.pdf>.
3. Lee, H., Kok, P. & Dowling, J. P. A quantum rosetta stone for interferometry. *Journal of Modern Optics* **49**, 2325–2338 (2002). URL <https://doi.org/10.1080/0950034021000011536>. <https://doi.org/10.1080/0950034021000011536>.
4. Flamini, F. *et al.* Thermally reconfigurable quantum photonic circuits at telecom wavelength by femtosecond laser micromachining. *Light: Science & Applications* **4**, e354–e354 (2015).
5. Pirandola, S., Eisert, J., Weedbrook, C., Furusawa, A. & Braunstein, S. L. Advances in quantum teleportation. *Nature Photonics* **9**, 641–652 (2015).
6. Xu, F. *et al.* Experimental quantum fingerprinting arXiv:1503.05499v1, [1503.05499v1](https://arxiv.org/abs/1503.05499v1).
7. Irvine, W. T. M., Lamas Linares, A., de Dood, M. J. A. & Bouwmeester, D. Optimal quantum cloning on a beam splitter. *Phys. Rev. Lett.* **92**, 047902 (2004). URL <https://link.aps.org/doi/10.1103/PhysRevLett.92.047902>.
8. Pan, J.-W. *et al.* Multiphoton entanglement and interferometry. *Rev. Mod. Phys.* **84**, 777–838 (2012). URL <https://link.aps.org/doi/10.1103/RevModPhys.84.777>.
9. Spring, J. B. *et al.* Boson sampling on a photonic chip. *Science* **339**, 798–801 (2013). URL <https://science.sciencemag.org/content/339/6121/798>.
10. Gariepy, G., Tonolini, F., Henderson, R., Leach, J. & Faccio, D. Detection and tracking of moving objects hidden from view. *Nature Photonics* **10**, 23–26 (2016).
11. Erskine, D. J. & Holmes, N. C. White-light velocimetry. *Nature* **377**, 317–320 (1995).
12. Höhn, D. Depolarization of a laser beam at 6328 Å due to atmospheric transmission. *Appl. Opt.* **8**, 367 (1969).
13. Bourgoin, J.-P. *et al.* Experimentally simulating quantum key distribution with ground-to-satellite channel losses and processing limitations (manuscript in preparation).
14. Sit, A. *et al.* High-dimensional intracity quantum cryptography with structured photons. *Optica* **4**, 1006–1010 (2017). URL <http://www.osapublishing.org/optica/abstract.cfm?URI=optica-4-9-1006>.
15. Paterson, C. Atmospheric turbulence and orbital angular momentum of single photons for optical communication. *Phys. Rev. Lett.* **94**, 153901 (2005). URL <https://link.aps.org/doi/10.1103/PhysRevLett.94.153901>.
16. Malik, M. *et al.* Influence of atmospheric turbulence on optical communications using orbital angular momentum for encoding. *Opt. Express* **20**, 13195–13200 (2012). URL <http://www.opticsexpress.org/abstract.cfm?URI=oe-20-12-13195>.
17. Brendel, J., Gisin, N., Tittel, W. & Zbinden, H. Pulsed energy-time entangled twin-photon source for quantum communication. *Phys. Rev. Lett.* **82**, 2594–2597 (1999). URL <https://link.aps.org/doi/10.1103/PhysRevLett.82.2594>.
18. Stucki, D., Brunner, N., Gisin, N., Scarani, V. & Zbinden, H. Fast and simple one-way quantum key distribution. *Appl. Phys. Lett.* **87**, 194108 (2005).
19. Townsend, P. D., Rarity, J. G. & Tapster, P. R. Single photon interference in 10 km long optical fibre interferometer. *Electron. Lett.* **29**, 634–635 (1993).
20. Muller, A. *et al.* “Plug and play” systems for quantum cryptography. *Appl. Phys. Lett.* **70**, 793–795 (1997).
21. Inoue, K., Waks, E. & Yamamoto, Y. Differential phase shift quantum key distribution. *Phys. Rev. Lett.* **89**, 037902 (2002).
22. Stucki, D. *et al.* High rate, long-distance quantum key distribution over 250 km of ultra low loss fibres. *New J. Phys.* **11**, 075003 (2009).
23. Jin, J. *et al.* Demonstration of analyzers for multimode photonic time-bin qubits. *Phys. Rev. A* **97**, 043847 (2018). URL <https://link.aps.org/doi/10.1103/PhysRevA.97.043847>.
24. Jin, J. *et al.* Genuine time-bin-encoded quantum key distribution over a turbulent depolarizing free-space channel. *Opt. Express* **27**, 37214 – 37223 (2019). URL <http://www.opticsexpress.org/abstract.cfm?URI=oe-27-26-37214>.
25. Vallone, G. *et al.* Interference at the single photon level along satellite-ground channels. *Phys. Rev. Lett.* **116**, 253601 (2016). URL <https://link.aps.org/doi/10.1103/PhysRevLett.116.253601>.
26. Cao, Y. *et al.* Long-distance free-space measurement-device-independent quantum key distribution [2006.05088](https://arxiv.org/abs/2006.05088).
27. Tan, K. & Cheng, X. Specular reflection effects elimination in terrestrial laser scanning intensity data using phong model. *Remote Sensing* **9** (2017). URL <https://www.mdpi.com/2072-4292/9/8/853>.

28. Bennett, C. H. & Brassard, G. Quantum cryptography: Public key distribution and coin tossing. In *Proceedings of IEEE International Conference on Computers, Systems, and Signal Processing*, 175–179 (IEEE Press, New York, Bangalore, India, 1984).
29. Lydersen, L. *et al.* Hacking commercial quantum cryptography systems by tailored bright illumination. *Nat. Photonics* **4**, 686–689 (2010).
30. Lydersen, L., Skaar, J. & Makarov, V. Tailored bright illumination attack on distributed-phase-reference protocols. *J. Mod. Opt.* **58**, 680–685 (2011).
31. Gras, G., Rusca, D., Zbinden, H. & Bussières, F. Countermeasure against quantum hacking using detection statistics [2010.08474](https://arxiv.org/abs/2010.08474).
32. Sajeed, S. *et al.* Security loophole in free-space quantum key distribution due to spatial-mode detector-efficiency mismatch. *Phys. Rev. A* **91**, 062301 (2015).
33. Agne, Sascha. *Exploration of Higher-Order Quantum Interference Landscapes*. Ph.D. thesis (2017). URL <http://hdl.handle.net/10012/12307>.

Methods

Detailed experimental setup

The experimental setup consists of two unbalanced Michelson interferometers (UMIs). The first UMI – *Converter* – creates the coherence while the second one – *Analyzer* – measures the coherence. The laser (Picoquant laser diode LDH 8-1-596, PDL-800B driver) emits 697 nm, 300ps multimode light pulses at a rate of 5MHz. Lights coming out of the multimode fiber are collimated and sent through the Converter. The path difference Δ_C between the long and short arms turns each incoming state into a coherent superposition of two time-bins separated by 0.57ns. They are sent towards the scattering surface and the scattered photons are collected by the Analyzer. The path difference between the short and the long arm in the Analyzer is Δ_A . A photon coming out of the Analyzer could have traversed one of the four possible paths: short-short (SS), short-long (SL), long-short (LS) and long-long (LL). If the path-differences in each UMI match, i.e., $\Delta_C \approx \Delta_A$, the probabilities of a photon coming via SL and LS paths become indistinguishable and result in interference. Piezoelectric crystals are placed in the short arm of each interferometer to adjust the path difference. The photons emerging from the Analyzer are focused into an SPDA containing 64 single-photon avalanche photo-diodes. The pixels of the SPDA are arranged in a 8×8 row-column configuration, with a pitch of $75 \mu\text{m}$. A focusing lens (Canon EF-S 18-200mm f/3.5-5.6) is used to illuminate the desired range of pixels with its focal length set to about 60 mm, thus yielding an angular resolution of 0.07° , and a total angular field of 0.5° .

Compensation for spatial mode distortion

A time-bin encoded photon entering an Analyzer with variable angle of incidence causes a lateral offset between the paths

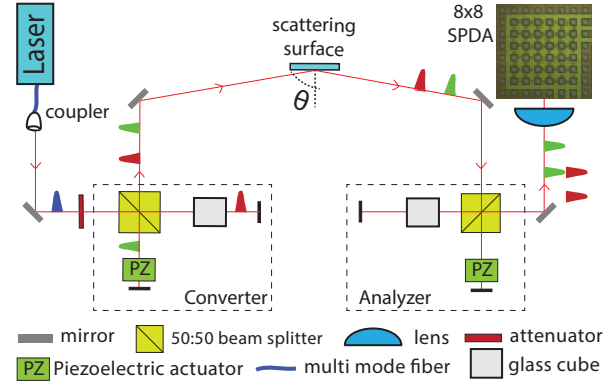


Figure 5. The experimental setup. The Converter creates two pulses separated by 0.6ns. The path difference between the two short-long (SL) and long-short (LS) pulses can be adjusted using the piezoelectric actuator placed in the short arm. A glass cube is present in the long arm of both interferometers to make the interferometers balanced in the spatial domain. The Analyzer recombines the pulses coming via SL and LS paths and the output is studied by the 8×8 SPDA. During the initial alignment, the incident angle $\theta = 25^\circ$ (figure not to scale).

impinging at the exit beam-splitter^{23,33} causing degradation of interference visibility. Channel induced spatial-mode distortions further lower the interference quality. The root cause of this is the inherent asymmetry of the unbalanced Michelson interferometers. A compensation technique is to use a glass material with appropriate length and refractive index to create a virtual mirror closer to the beamsplitter. In this way, the interferometer, although asymmetric in time, becomes symmetric in the spatial-mode domain. We placed a 118 mm-long glass cube with refractive index 1.4825 at the long arm to match the distance between beam-splitter-to-virtual-mirror with the short arm (see³³ for more details and the analytical formula). This compensation not only improves performance at higher AOI, but is also necessary to enable high interference visibility with a multimode beam.

Correlation of patterns

Here we describe the method by which Fig. 4e was plotted. Figure 6a shows the same image (right) along with the observed visibility (left) across all the SPDA pixels. The visibility was calculated as $V = (I_{max} - i_{min}) / (I_{max} + I_{min})$ where I_{max} (I_{min}) is the maximum (minimum) count in a phase-signature cycle. Pixel (1, 1) was the trigger, and (1, 2), (2, 2) and (5, 8) had very high dark counts. The observed pattern at these three defected pixels are shown in Figure 6b where no correlation with the reference pattern was visible. Fig. c shows the observed pattern at the bottom six pixels of column 4. The resemblance with the *reference pattern* was quite pronounced. On the other hand, fig d shows the observed patterns for the bottom three pixels of column 1 that detected relatively fewer number of photons and are much more distorted.

They are in the middle of the two previous extremes and the correlation value with the reference pattern for them lies in the middle. Before calculating the cross-correlation, both the reference and observed patterns were shifted downward by 0.5 for the ease of analysis.

The single-photon-detector-array sensor

The SPDA camera is composed of 64 single photon avalanche diodes arranged in a square pattern with 8 rows and 8 columns. Each row and column has eight $30\mu\text{m}$ diameter detectors with X and Y pitch equal to $75\mu\text{m}$. The average dark count rate was 35 cps, deadtime was 150 ns and the timing resolution was 100ps. The electrical output from the camera (Samtec Cable, SEAC-30-08-XX.X-TU-TU-2) contains 64 LVDS detection signal from the pixels along with other control signals. An adapter board was designed to match the electrical signal interface of the camera to that of the time tagger (Universal quantum devices) as shown in Fig. 7. The developed board translates the 64 LVDS camera outputs into four groups of 16 LVDS channels going into the time-tagger. As a result, time stamps from the camera can be read by the tagger at a rate of approximately 1 GTag/s through an external-PCI-express interface. The adapter board provide the option to sacrifice upto four pixels (1, 8, 58 and 64) to be used as external trigger. In this work only one trigger was used. When triggering is not required, the pixels can function as normal detectors.

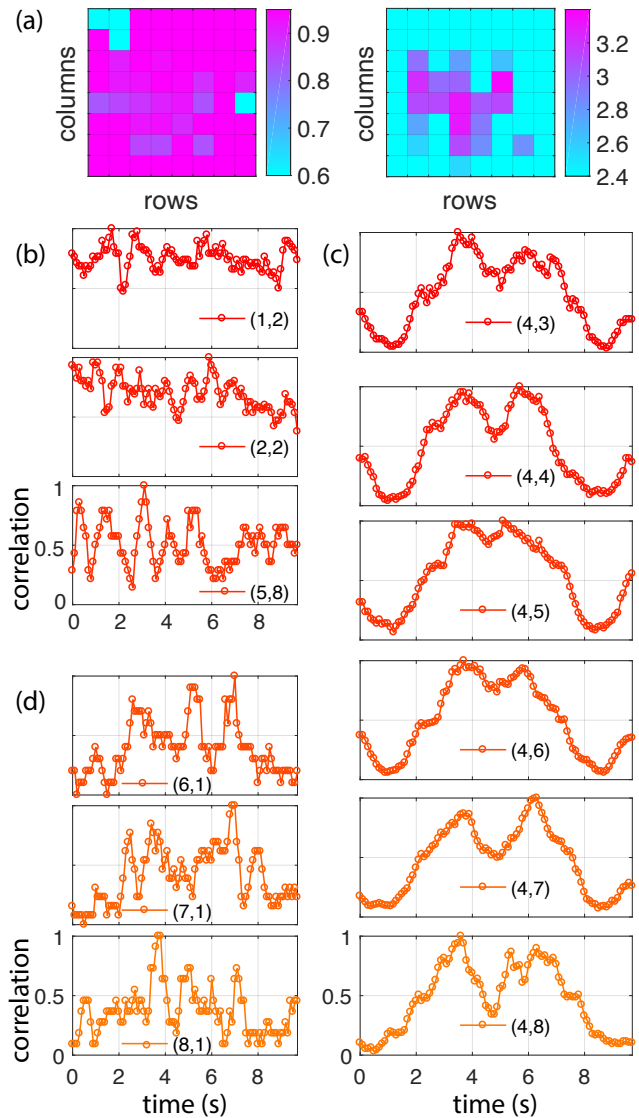


Figure 6. Visibility and patterns observed at different pixels of the SPDA imager. a. visibility across all the pixels (left) and the reconstructed image drawn from correlation (right) b. observed pattern at the three defective pixels having high dark counts. The correlation with the reference pattern is lower than threshold. c. observed pattern at the bottom six pixels of column four. The correlation with the reference pattern is higher than the threshold. d. observed pattern at bottom three pixels of column one. The correlation with the reference pattern is between the two previous extremes but still lower than the chosen threshold. By plotting the pixels with correlation higher than the threshold, the image was reconstructed with enhanced contrast as shown in fig a (right).

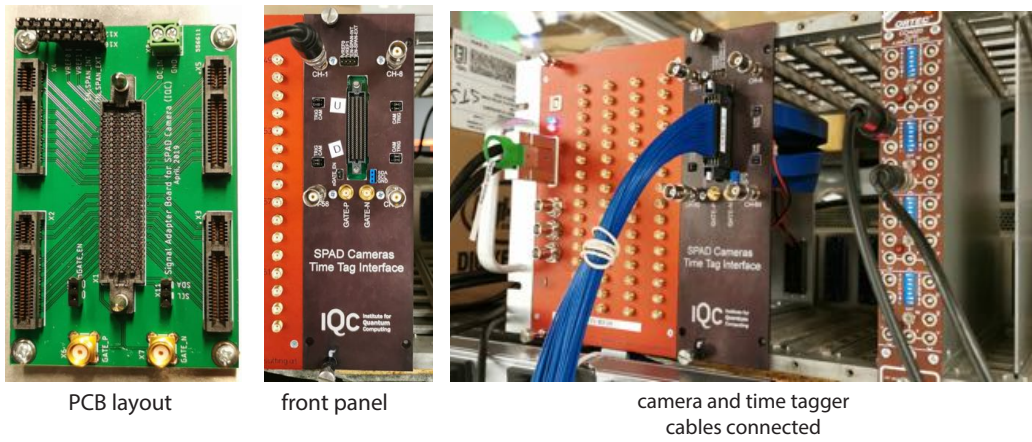


Figure 7. Interface board. The camera output (64 LVDS pairs) are linked to an interface board, and divides the signals to 4 blocks of 16 LVDS pairs, as well as provides control signal inputs. The 4 signal blocks are directly interfaced with a high-speed time-tagger that can handle 64 input channels, up to 1 GTag/s.